A Computational Study of the Interfacial Structure and Capacitance of Graphene in [BMIM][PF_6] Ionic Liquid

Eunsu Paek, Alexander J. Pak and Gyeong S. Hwang

J. Electrochem. Soc. 2013, Volume 160, Issue 1, Pages A1-A10.
doi: 10.1149/2.019301jes

Journal of The Electrochemical Society, **160** (1) A1-A10 (2013)
0013-4651/2013/160(1)/A1/10/$28.00 © The Electrochemical Society

A Computational Study of the Interfacial Structure and Capacitance of Graphene in [BMIM][PF_6] Ionic Liquid

Eunsu Paek, Alexander J. Pak, and Gyeong S. Hwang[z]

Department of Chemical Engineering, University of Texas, Austin, Texas 78712, USA

A combination of graphene-like electrodes and ionic liquid (IL) electrolytes has emerged as a viable and attractive choice for electrochemical double layer (EDL) capacitors. Based on combined classical molecular dynamics and density functional theory calculations, we present the interfacial capacitance between planar graphene and [BMIM][PF_6] IL, with particular attention to the relative contributions of the electric double layer capacitance at the graphene/IL interface and the quantum capacitance of graphene. The microstructure of [BMIM][PF_6] near the graphene electrode with varying charge densities are investigated to provide a molecular description of EDLs, including BMIM/PF_6 packing and orientation, cation-anion segregation, and electrode charge screening. Although the IL interfacial structures exhibit an alternative cation/anion layering extending a few nanometers, the calculated potential profiles provide evidence of one-ion thick compact EDL formation. The capacitance-potential curve of the EDL is convex- or bell-shaped, whereas the quantum capacitance of graphene is found to have concave- or U-shaped characteristics with a minimum of nearly zero. Consequently, we find that the total interfacial capacitance exhibits a U-shaped trend, consistent with existing experimental observations at a typical carbon/IL interface. Our work highlights the importance of the quantum capacitance in the overall performance of graphene-based EDL capacitors.
 [DOI: 10.1149/2.019301jes]

Manuscript submitted July 23, 2012; revised manuscript received October 11, 2012. Published November 6, 2012.

Ionic liquids (ILs) are a relatively new class of materials with many unique and useful properties. They exist in the liquid state at room temperature, and exhibit high thermal and chemical stability, extremely low volatility, non-flammability, and wide electrochemical windows.[1,2] The IL's properties are highly tunable through the choice of the cation and anion pair.[3] Over recent years, room temperature ILs have received considerable research attention due to their broad range of potential applications.[4] In particular, the ionic nature of ILs makes them an excellent choice for "solvent-free" electrolytes in electrochemical double layer capacitors (EDLCs) or supercapacitors.[5,6]

The performance of EDLCs is largely determined by the microstructure and capacitance of the electrical double layers (EDLs) at the interface between ILs and electrodes. Hence, recently the structure and behavior of ILs in the vicinity of electrified surfaces have been studied using a variety of experimental and theoretical techniques.[7–11] The IL ions are found to be alternatively stacked near a charged electrode due to strong electrode-ion and ion-ion electrostatic interactions;[8–10] the distinct alternative layering can be possible by the fact that solvent-free dense ILs typically have a small Debye length on the order of ion size.[12] Although the layered structure tends to extend up to a few nanometers, several previous studies[7] suggest that the EDL potential drop mainly occurs within the first layer of counterions (which is typically 3–5 Å thick). The interfacial behavior is hardly explained by the standard Gouy-Chapman-Stern (GCS) model[13] of dilute aqueous electrolytes in which the EDL is typically composed of a compact inner layer and a diffuse outer layer.

Besides the interfacial structure of ILs, the differential EDL capacitance in ILs has been extensively measured and characterized. The capacitance-potential (C–ϕ) curve for ILs with metal electrodes commonly shows a convex parabolic shape with one maximum or two local maxima, which is the so-called bell-shaped or camel-shaped curve.[14–17] On the other hand, in aqueous electrolytes the EDL capacitance is known to exhibit a minimum near the potential of zero charge (PZC) and increases with applied electrode potential, yielding a concave or U-shaped C–ϕ curve.[13] Kornyshev[18] derived an elegant analytical expression based on the Poisson-Boltzmann lattice-gas model which suggested that the C–ϕ curve shape can be a function of void fraction, or compressibility, near the electrolyte-electrode interface. His work inspired many attempts to explain the C–ϕ curves in various shapes. Molecular-level computer simulations have been used to examine the relationship between the capacitance and microstructure of EDLs.[10,19–21] Earlier studies[22–25] tend to well capture the general trends in the formation of an EDL in response to an applied electrode potential. However, they have also shown that the EDL structure and capacitance can be a complex function of many factors such as the size, configuration and polarizability of ions, the effective dielectric constant in the electrolyte solution, and the non-electrostatic interaction of ions with the electrode surface, which are not yet clearly understood; this leaves room for further investigation.

Carbon-based nanomaterials (such as porous carbon, carbon nanotubes, and graphene) have been regarded as viable candidates for supercapacitor electrodes due to their high surface area and good electrical conductivity. As suggested by recent computational studies, the EDL capacitance in ILs with carbon-based electrodes can be significantly influenced by the shape and surface topology of the electrode.[26–29] In addition, some experimental efforts have been made to enhance the capacitance of carbon-based EDLCs through electrode doping and functionalization.[30–32] At a semiconductor (or semimetallic) electrode-electrolyte interface, the space charge layer within the electrode may act as a capacitor in series with the EDL;[33–35] likewise, at the IL/carbon interface the carbon electrode capacitance might need to be taken into account for the interfacial capacitance. Randin and Yeager[33] first applied the semiconductor "space charge" capacitance picture for graphite with NaF. Gerischer et al.[36,37] later amended this theory to incorporate the electronic density of states (DOS) of graphite within the framework of semiconductor theory; their analysis suggested that the finite DOS of graphite near the Fermi level resulted in the dominance of the space charge contribution to the measured capacitance. Luryi,[38] however, first formalized the concept of quantum capacitance for low-dimensional materials such as graphene and metallic carbon nanotubes, in which the space charge treatment is inapplicable. The quantum capacitance of carbon nanostructures is directly proportional to the DOS, and can thus be altered by tuning the electronic structure through doping, functionalization, and mechanical deformation. This may suggest that the previously observed improvements in capacitor performance from the chemical and/or mechanical modifications of carbon-based electrodes could be attributed to the enhancement in not only EDL capacitance but also quantum capacitance. Despite its importance, the relative role played by electrode and EDL in determining the interfacial capacitance still remains unclear.

In this work, we examine the interfacial capacitance and structure of graphene in IL 1-butyl-3-methyl-imidazolium hexafluorophosphate ([BMIM][PF_6]) using a combination of classical molecular dynamics (MD) and density functional theory (DFT) calculations. Our particular interest lies in understanding the relative contributions of EDL capacitance and quantum capacitance to the total interfacial capacitance between graphene and [BMIM][PF_6]. First, we investigate the microstructure of [BMIM][PF_6] near the graphene electrode by varying

[z]E-mail: gshwang@che.utexas.edu

the electrode surface charge using MD simulations, and use the calculated distributions of BMIM and PF_6 ions to evaluate the potential variations in [BMIM][PF_6] and successively EDL differential capacitances. Then, we employ DFT calculations to estimate the quantum capacitance of pristine graphene with a brief comparison to theoretically predicted and experimentally estimated values. While the total capacitance at the graphene/IL interface is given as a series of the EDL capacitance and the quantum capacitance, our work clearly demonstrates that the quantum capacitance can play a major role in determining the overall performance of graphene/IL-based supercapacitors.

Computational Methods

Force fields.— Success of classical MD simulations strongly depends on the reliability of the force fields (FFs) used. For ILs, all-atom (AA) and united-atom (UA) FFs have been employed, depending on the type of information sought. The AA model describes all atoms explicitly, whereas the UA model treats a group of atoms as a single 'united' atom, such as methyl (CH_3) and methylene (CH_2) groups as single interaction centers. Computationally less expensive UA-FFs permit larger-size and longer-time simulations than AA-FFs, but they are limited in their ability to describe configurations of atoms in detail, particularly in the interfacial region. In this work, we employed AA-FFs in the frame of OPLS-AA[39,40] (Optimized Potential for Liquid Simulations/All Atom), as an explicit description of the electrolyte-electrode interface is necessary.

In the FF formulation, the total energy (E_{total}) of a given system is expressed as the sum of bonding (E_{bond}, E_{angle}, $E_{torsion}$) and pair-wise nonbonding ($E_{nonbond}$) energies. The nonbonding contribution includes the Coulomb interaction of partial atomic charges and the van der Waals (vdW) interaction in the 12-6 Lennard-Jones (L-J) form.

$$
\begin{aligned}
E_{total} &= E_{bond} + E_{angle} + E_{torsion} + E_{nonbond} \\
E_{bond} &= \sum_i k_{b,i}(r_i - r_{0,i})^2 \\
E_{angle} &= \sum_i k_{\theta,i}(\theta_i - \theta_{0,i})^2 \\
E_{torsion} &= \sum_i \left[\frac{V_{1,i}}{2}(1+\cos\phi_i) + \frac{V_{2,i}}{2}(1-\cos 2\phi_i) \right. \\
&\quad \left. + \frac{V_{3,i}}{2}(1+\cos 3\phi_i) + \frac{V_{4,i}}{2}(1-\cos 4\phi_i) \right] \\
E_{nonbond} &= \sum_i \sum_{j>i} \left\{ \frac{q_i q_j e^2}{r_{ij}} + 4\varepsilon_{ij} \left[\left(\frac{\sigma_{ij}}{r_{ij}}\right)^{12} - \left(\frac{\sigma_{ij}}{r_{ij}}\right)^{6} \right] \right\}
\end{aligned}
\qquad [1]
$$

Here, $k_{b,i}$, $k_{\theta,i}$ and $V_{n,i}$ represent the bond, angle, and torsion force constants, respectively; $r_{0,i}$ and $\theta_{0,i}$ are the bond distance and the bond angle at equilibrium, respectively. For $E_{nonbond}$, q_i is the partial atomic charge, r_{ij} is the distance between atoms i and j, ε_{ij} and σ_{ij} are the L-J parameters which refers to the depth of the potential well and the distance in units of radii where the potential is zero, respectively. The Coulomb and L-J energies were calculated between atoms in different molecules or atoms in the same molecule separated by at least three bonds. The L-J parameters for unlike atoms were obtained from the Lorentz-Berthelot combination rule, i.e., $\varepsilon_{ij} = \sqrt{\varepsilon_{ij}\varepsilon_{jj}}$ and $\sigma_{ij} = (\sigma_{ii} + \sigma_{jj})/2$. We used the FF parameters for [BMIM][PF_6] from Pádua et al.,[41,42] while allowing PF_6 to be fully flexible based on the geometrical parameters from Borodin et al.[43] The L-J parameters of graphene are from Battezzati et al.[44] To confirm the validity of the FFs, we calculated the bulk density of [BMIM][PF_6] for 500 ion pairs in a cubic box; the predicted density is 1.33 g/cm^3 at $P = 1$ atm and $T = 300$ K, which is in good agreement with previous experiments[45] (1.36 g/cm^3) and calculations[46,47] (1.32−1.35 g/cm^3).

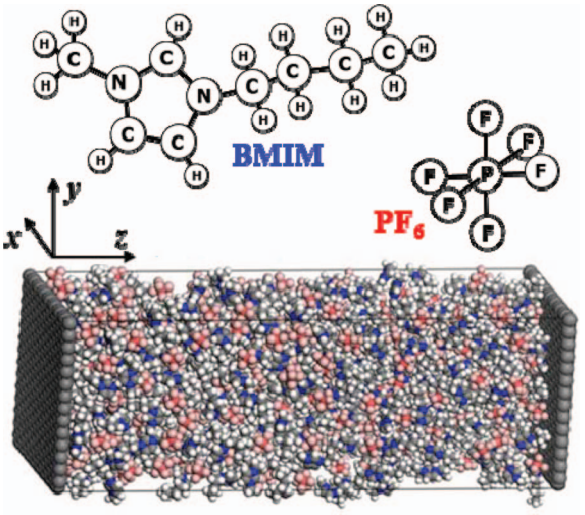

Figure 1. Schematic of BMIM, PF_6, and the simulation box. Planar graphene sheets are placed at the two ends of the simulation domain. White, blue, and grey balls indicate H, N, and C atoms in BMIM, and red and pink balls indicate P and F atoms in PF_6. Periodic boundary conditions are applied in the x and y directions.

Molecular dynamics simulations.— Figure 1 shows a schematic of the simulation system which consists of [BMIM][PF_6] ion pairs bounded between two graphene electrodes. The lateral size of the graphene sheets is 34.18 × 34.53 Å^2, corresponding to 448 C atoms. The distance between the electrodes ($d_{Gr\text{-}Gr}$) was chosen large enough such that the bulk properties of [BMIM][PF_6] IL were reached in the middle region of the system for various electrode excess charge densities (σ); it turns out that $d_{Gr\text{-}Gr}$ = 70 Å is sufficient when σ ≤ 7 μC/cm^2, while $d_{Gr\text{-}Gr}$ = 100 Å at σ ≥ 8 μC/cm^2.

Initially, 213 [BMIM][PF_6] pairs for $d_{Gr\text{-}Gr}$ = 70 Å (346 pairs for $d_{Gr\text{-}Gr}$ = 100 Å) were randomly placed in a three-dimensional (3D) domain with dimensions of 37.6 × 38 × 64 Å^3; periodic boundary conditions were imposed in the x and y directions. The x and y dimensions were slowly decreased to the target value of 34.18 × 34.53 Å^2 (which is equal to the lateral size of graphene) over 500 ps. Then, the graphene electrodes were inserted at 3 Å above and below the [BMIM][PF_6] IL domain. All MD simulations reported herein employed the velocity Verlet algorithm[48] to integrate Newton's equation of motion with a time step of 1 fs.

We first ran MD at 1000 K for 1.2 ns, followed by 3 ns at 300 K to equilibrate the system. Production runs were carried out for 4 ns with atomic positions recorded every 4 ps. All runs were in the *NVT* ensemble with the temperature controlled by a Nose-Hoover thermostat[49] with a 100 fs damping parameter. Graphene sheets were kept rigid, and the C-H bonds in BMIM were constrained using the Shake algorithm.[50] We used spherical cutoff radii of 12 Å and 16 Å for the vdW and Coulomb interactions, respectively. Electrostatic interactions beyond the cutoff radius of 16 Å were calculated using a particle-particle particle-mesh (PPPM) scheme[51] in reciprocal space; the inter-slab interactions in the z direction were removed by inserting a large vacuum space between the graphene sheets.[52] All MD simulations were performed with the Large-scale Atomic/Molecular Massively Parallel Simulator (LAMMPS) program.[53] All MD results reported herein were obtained from the average of five independent simulations with different initial atomic configurations.

Density functional theory calculations.— Our DFT calculations were performed within the Perdew-Wang 91 generalized gradient approximation (GGA-PW91),[54] using the Vienna Ab initio Simulation Package (VASP).[55] We employed the projector augmented wave (PAW) method to describe the interaction between core and valence

electrons,[56] and a planewave basis set with a kinetic energy cutoff of 400 eV. For the electronic structure calculation of pristine graphene, we used a 4-atom rectangular sheet with dimensions of 4.272 × 2.466 Å^2; here, the GGA-optimized lattice constant of 2.466 Å was employed, which is slightly larger than the experimental value of 2.461 Å. Periodic boundary conditions were employed in all three directions with a vacuum gap of 10 Å in the vertical (z) direction to separate the system from its periodic images. A (21 × 21 × 1) k-point grid in the scheme of Monkhorst-Pack[57] was used for the Brillouin zone sampling.

Results and Discussion

Distribution of IL ions near uncharged graphene surfaces.— Figure 2 shows the mass density profiles of BMIM and PF_6 (with a bin size of 0.1 Å) along the direction normal to the graphene surface. The profiles exhibit noticeable oscillations which dampen away from the electrode; the layering behavior is found to extend about 25–30 Å after which the IL structure becomes nearly bulk-like. The first layer that starts around 2.6 Å from the electrode has an average density of 1.59 g/cm^3 which is about 20% greater than the bulk density of 1.33 g/cm^3. The average densities of the second and third layers are predicted to be 1.33 g/cm^3 and 1.29 g/cm^3, respectively, while their respective peak densities are 1.5 and 1.1 times larger than the bulk density, respectively.

The oscillations are indicative of layered IL structure formation at the interface, as also suggested by previous studies.[21,46,47,58] This is apparently attributed to the vdW force that draws IL ions close to the graphene surface, leading to the formation of the first IL layer where BMIM and PF_6 are packed together to maximize the IL-graphene vdW interaction. A detailed analysis of the atomic arrangement of BMIM and PF_6 will follow.

According to our calculations, the predicted vdW energy of 11 kcal/mol for the BMIM-graphene interaction tends to be substantially larger than 5 kcal/mol for the PF_6-graphene interaction; however, in the first layer BMIM and PF_6 are maintained at the same number density (~5.6 × 10^{-3} Å^{-3}) to satisfy the condition of charge neutrality. It is also worth noting that the strength of vdW energies is an order of magnitude greater than the thermal energy at room temperature (kT ≈ 0.59 kcal/mol); hence, the first-layer ions are expected to have a rather rigid, or solid-like, structure due to suppression of their thermal fluctuations. In comparison, at an IL/vacuum interface, ions may also rearrange to reduce the surface free energy, but only a marginal increase in the surface layer number density without distinct layering is observed.[59,60]

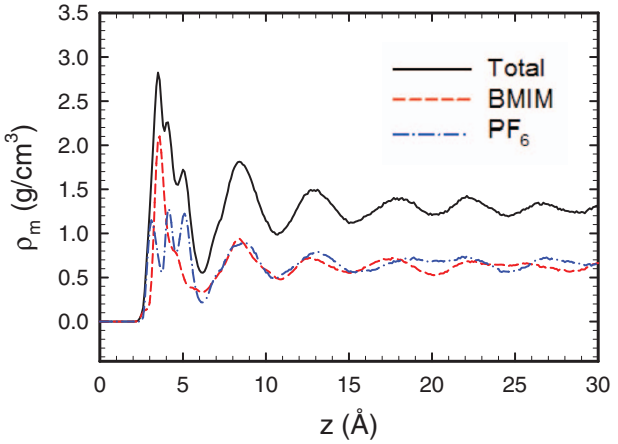

Figure 2. Total, BMIM, and PF_6 mass density (ρ_m) profiles along the z-axis near an uncharged graphene electrode which is located at $z = 0$.

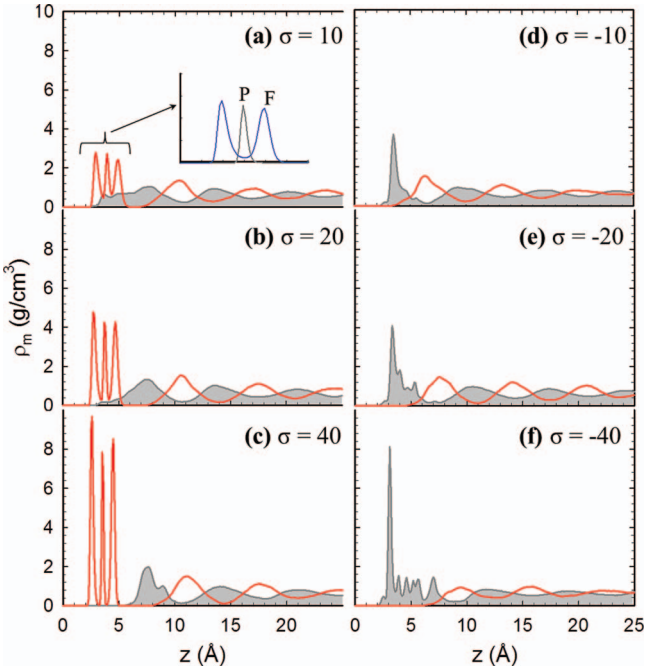

Figure 3. BMIM and PF_6 mass density (ρ_m) profiles along the z-axis near charged graphene electrodes with different excess charge densities (σ) as specified (in μC/cm^2). Each electrode is located at $z = 0$. The inset in (a) shows the distributions of F and P atoms.

Distribution of IL ions near charged graphene surfaces.— To emulate the charged electrodes, we assigned excess positive (negative) charge equally to the C atoms in graphene located at $z = 0$ Å ($z = 70$ or 100 Å); here, the excess charge density was varied from σ = ±1 to ±60 μC/cm^2 (specific values for σ are indicated by the circles in Fig. 11). A charged electrode creates an electric field, which causes the rearrangement of IL ions near the electrode to screen the electric field. Figure 3 shows how the electrode charging influences the distribution of BMIM and PF_6; as the electrode is increasingly charged, the segregation between BMIM and PF_6 accordingly increases. When the electrode is positively charged [Fig. 3a–3c], anionic PF_6 is attracted while cationic BMIM is repelled. At σ = +10 μC/cm^2 [(a)], BMIM still remains partially mixed with the PF_6 first layer. However, at σ = +40 μC/cm^2 [(c)], BMIM is clearly segregated from the PF_6 layer. Similarly, PF_6 forms a second layer with some mixing in the BMIM first layer when σ = −10 μC/cm^2 [(d)]. When σ = −40 μC/cm^2 [(f)], PF_6 has a more distinct layer with a smaller degree of mixing. More quantitative analysis of the degree of mixing will be discussed later.

The alternative layering of PF_6 and BMIM is apparently due to the electrostatic interaction between them. For instance, BMIM cations, which accumulate near the negative electrode, attract PF_6 anions; this process repeats to form multi-stacked alternatingly charged layers. As illustrated in Fig. 3, the distinct multi-layering is found to extend about 3 nm from a charged electrode, while the thickness of each alternating [BMIM][PF_6] layer tends to be 7–9 Å; overall, the results are consistent with previous experimental observations of the ordering of ILs in the vicinity of various charged surfaces.[8,61,62]

For the same amount of electrode charge |σ|, as shown in Fig. 3, the PF_6 density near the positive electrode is consistently greater than the BMIM density near the negative electrode. At |σ| = 10 μC/cm^2, the first-layer PF_6 density (=1.45 g/cm^3) is 113% greater than the bulk PF_6 density (=0.68 g/cm^3), whereas the first-layer BMIM density (=0.87 g/cm^3) is only 34% greater than the bulk BMIM density (=0.65 g/cm^3). At |σ| = 40 μC/cm^2, the first-layer densities of PF_6 and BMIM are 312% and 116% greater than their respective bulk densities [Table I].

Figure 4 depicts the arrangement of counterions in the first layer for various σ. The snapshots clearly demonstrate that PF_6 accumulates

Table I. Predicted peak and average densities of counterions in the first IL layer from electrodes with different charge densities.

σ [μC/cm^2]	ρ_{max} [g/cm^3]	ρ_{avg} [g/cm^3]
10	2.75	1.45
20	4.78	1.90
40	9.68	2.80
−10	3.70	0.87
−20	4.09	0.99
−40	8.12	1.69

more densely than BMIM, which is due to their steric differences. The smaller size of PF_6 allows them to pack more tightly than BMIM; moreover, PF_6 can pack into a well-ordered lattice-like structure due to its highly symmetric compact configuration, unlike BMIM with a rather complex geometry.

The rearrangement of ions in response to the excess electrode charge causes the interfacial space charge density to deviate from the neutral case. Figure 5 shows the space charge density profiles attributed to the respective ion species along the direction normal to the electrode with varying σ, as calculated from the number densities and partial charges of each atom; each profile features fluctuations near the electrodes which gradually dampen until nearly flat in the bulk region. Near the positive electrodes [(a)–(c)], the negative (positive) sharp peaks correspond to planarly-aligned negatively-charged F (positively-charged P) atoms in PF_6. The comparatively broadened fluctuations near the negative electrodes [(d)–(f)] reflect the relatively even partial charge distribution over the atoms in the BMIM ring, as detailed later. Overall, the positive/negative charge densities are proportional to the number densities of [BMIM][PF_6] molecules, as the charges on PF_6 and BMIM are equal in magnitude (±1).

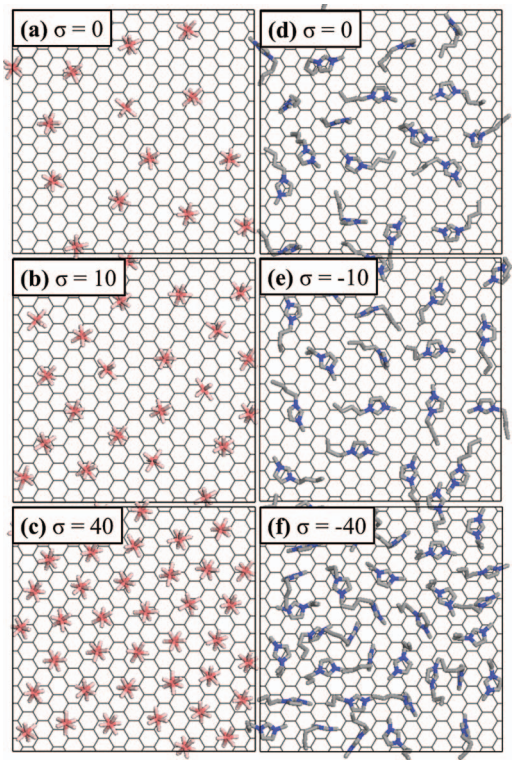

Figure 4. Snapshots of counterions in the layer closest to charged electrodes with different excess charge densities as specified (in μC/cm^2); (a)-(c) PF_6, (d)-(f) BMIM. Thin grey lines depict the graphene lattice, and red/pink clusters (left panels) and grey/blue sticks (right panels) represent PF_6 and BMIM, respectively.

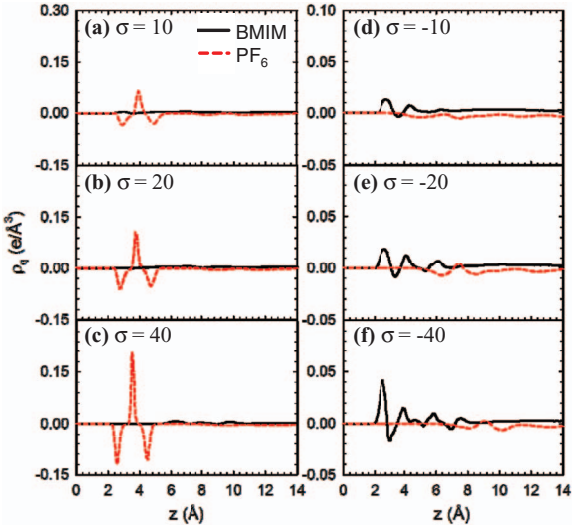

Figure 5. Space charge density (ρ_q) profiles due to BMIM and PF_6 along the z-axis near charged electrodes with different excess charge densities as specified (in μC/cm^2). Each electrode is located at $z = 0$.

Electrode charge screening and cation-anion segregation.— Table II summarizes[63] the net charge (q_{net}) densities of the first layers for various σ, together with corresponding positive (q_+) and negative (q_-) charge densities. We assessed how well the first layer of ions (counterion-rich) screens the electrode charge using a screening parameter $\beta = -q_{net}/\sigma$; that is, if $\beta > 1$ the electrode charge is overscreened. According to this analysis, both positive and negative electrodes tend to be overshielded by the first-layer ions unless σ is fairly large (>50 μC/cm^2).

For a given |σ|, the PF_6-rich layer is found to overscreen more than the BMIM-rich layer; note that the β values are 1.84 and 1.29, respectively, at σ = +10 and −10 μC/cm^2. This is related to the packing efficiency difference between PF_6 and BMIM, i.e., smaller PF_6 ions are crowded into the first layer more effectively than larger BMIM ions, as also indicated by the mass density profiles [Fig. 3].

As |σ| increases, the packing density of counterions in the first layer approaches an asymptote defined by steric limitations. Once this limit is reached (σ > 50 μC/cm^2), additional counterions form a second layer. Hence, β decreases as |σ| increases until both the PF_6 and BMIM layer have β < 1, i.e., the electrode is underscreened by the first layer. At this limit, PF_6 is found to have a greater packing density than BMIM, as β for the PF_6 layer is greater than that of the BMIM layer.

We also estimated the degree of [BMIM][PF_6] segregation in the first layer by defining a counterion mixing parameter, $\chi = q_{+/-}/(q_{+/-} + q_{-/+})$; that is, χ is the ratio of counterions to total number of ions (χ = 1 if BMIM and PF_6 are completely separated). As summarized

Table II. Charge densities ($q_{net} = q_- + q_+$), screening parameter (β), and counterion mixing parameter (χ) in the first counterion layer from electrodes with different charge densities.

σ (μC/cm^2)	q_{net} (μC/cm^2)	q_- (μC/cm^2)	q_+ (μC/cm^2)	β	χ
10	−18.4	−26.9	8.5	1.84	0.68
20	−32.0	−37.5	5.5	1.60	0.85
40	−53.9	−53.9	0.0	1.35	1.00
100	−85.3	−85.3	0.0	0.85	1.00
−10	12.9	−7.1	20.0	1.29	0.65
−20	25.1	−0.5	25.6	1.25	0.98
−40	44.6	−0.4	45.0	1.11	0.99
−100	67.2	−0.0	67.2	0.67	1.00

in Table II, PF_6 and BMIM tend to mix together at small σ but segregate at large σ. When $\sigma = \pm 10$ μC/cm^2, the first layers at both electrodes have around 65–68% counterions. As σ increases, however, χ increases until the first layer is 100% counterions, as predicted by the mass density profiles [Fig. 3]. This is apparently attributed to the strong electrostatic attraction (repulsion) of the counterion (coion) with the electrode. Interestingly, χ approaches unity more rapidly for BMIM than PF_6; it turns out that BMIM tends to reorient and sterically prevent PF_6 from mixing with BMIM, as discussed in more detail later.

Orientation of IL ions near uncharged graphene surfaces.— As illustrated in the inset of Fig. 3a, PF_6 arranges to form two planes (each of which is made of three F atoms) parallel to the flat electrode. In this orientation, the three F atoms maximize their vdW interactions with graphene, making this the preferred orientation. The density profile of PF_6 shows a single peak at the second and third layers, indicating that the preferred orientation no longer exists. The first layer of BMIM exhibits a single distinct peak, implying its tendency to lie parallel to the electrode.

The BMIM orientation in the first layer was analyzed in more detail using an order parameter, $P_2(\cos\theta) = \langle(3\cos^2\theta - 1)/2\rangle$; the results are shown in Fig. 6. Here, θ is the angle of the orientation of the ring plane (or butyl chain) with respect to the electrode surface normal. The order parameter (which ranges from −0.5 to 1.0) provides important information about orientation preferences; for instance, $P_2(\cos\theta) = 1$ at $\theta = 0°$, $P_2(\cos\theta) = -0.5$ at $\theta = 90°$, and $P_2(\cos\theta) \approx 0$ if there is no preferred orientation. In the first layer, the peak value for the ring plane is −0.5, indicating that the electrode and the imidazole ring of BMIM are parallel. In addition, the value of about −0.5 for the butyl chain implies that it is parallel as well. This is not surprising since the parallel orientation leads to the maximum vdW interaction between BMIM and graphene. At the transition ($z \approx 6$ Å) from the first to second layer, the ring plane value rises and shows a maximum of about 0.45; this implies that the ring plane tends to lie tilted to the electrode surface. In the second layer ($z \approx 8$ Å), the decreased ring plane value (≈ −0.2) indicates that the imidazole ring still has a small tendency to lie flat; however, after the third layer, the orientation preference disappears. Our results are in good agreement with previous theoretical[21,46,47,58,64] and experimental[65] studies.

Orientation of IL ions near charged graphene surfaces.— As expected, the orientation of PF_6 near the positive electrode is found to be analogous to the uncharged electrode case; the additional electrostatic attraction with negatively charged F atoms causes the three PF_6 peaks to become more pronounced, as also seen in the corresponding mass density profiles [Fig. 3]. On the other hand, near the negative electrode, PF_6 shows only one broad peak, indicating that PF_6 loses its preferred orientation.

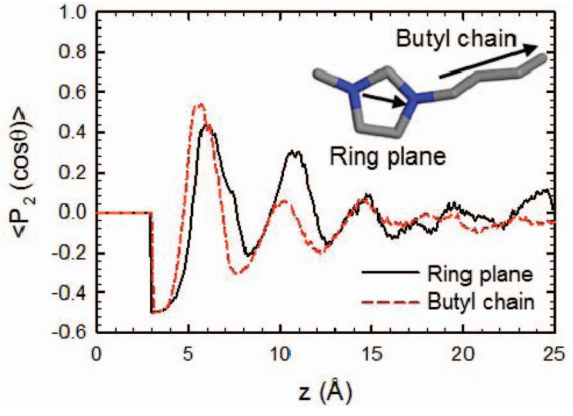

Figure 6. Order parameter <$P_2(\cos\theta)$> profiles for BMIM along the *z*-axis for the angles of the ring plane and butyl chain with respect to the graphene surface normal.

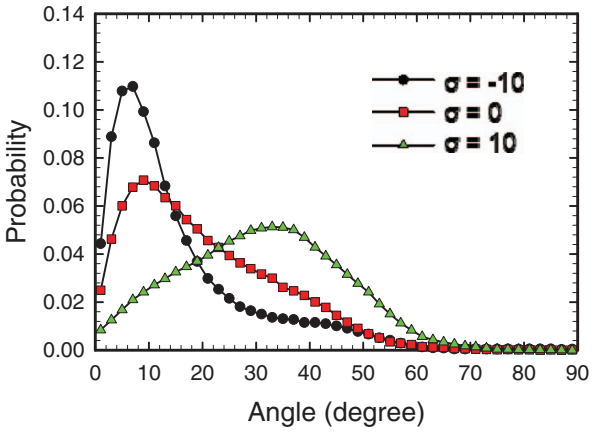

Figure 7. Probability distributions for the BMIM ring normal angle with respect to the graphene surface normal in the first IL layer at varying electrode charge as specified (in μC/cm^2).

The ring orientation of BMIM in the first layer may vary between 0° and 90°. Figure 7 shows the distributions of the BMIM ring orientations[66] when $\sigma = 0$ and ± 10 μC/cm^2. For $\sigma = 0$ μC/cm^2, the maximum probability occurs around 10°. The distribution becomes narrower (broader) with the maximum probability around 5° (25–40°) when the electrode is negatively (positively) charged. This suggests that the additional electrostatic attraction enhances the tendency of the BMIM ring to lie parallel to the negative electrode, which has also been observed experimentally;[67,68] recall that the BMIM ring is positively charged. Conversely, the electrostatic repulsion causes the BMIM ring to tilt away from the electrode. We also examined the ring orientation distribution for $\sigma = -40$ μC/cm^2 in Fig. 8. In the highly charged case, as shown in the inset of Fig. 8, the BMIM ring distribution exhibits two distinct features – a sharp peak [indicated by (a)] followed by a broad peak [(b)]; it seems that BMIM has two types of ring orientations, as seen in Fig. 8. In the (a) layer (closest to the electrode), rings have the expected preference to lie parallel to the electrode, with around 85% of rings less than 10°. The rings in the (b) layer, however, exhibit a relatively level distribution which suggests that the rings are tilted with no preferred orientation.

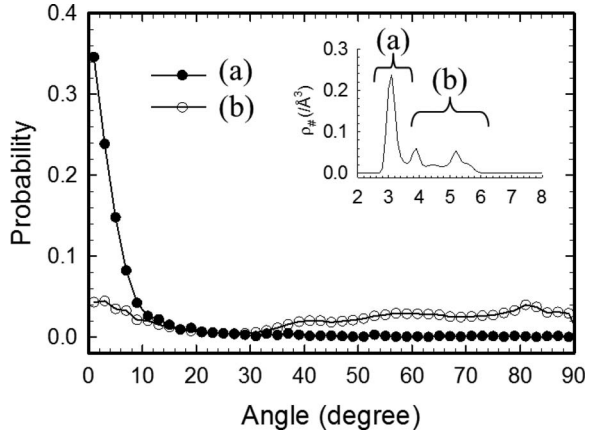

Figure 8. Probability distribution for the BMIM ring normal angle with respect to the graphene surface normal in the BMIM layer adjacent to a negatively charged graphene at $\sigma = -40$ μC/cm^2. The inset shows the corresponding number density profile of the BMIM ring atoms, suggesting that BMIM forms two sub-layers as indicated by (a) and (b).

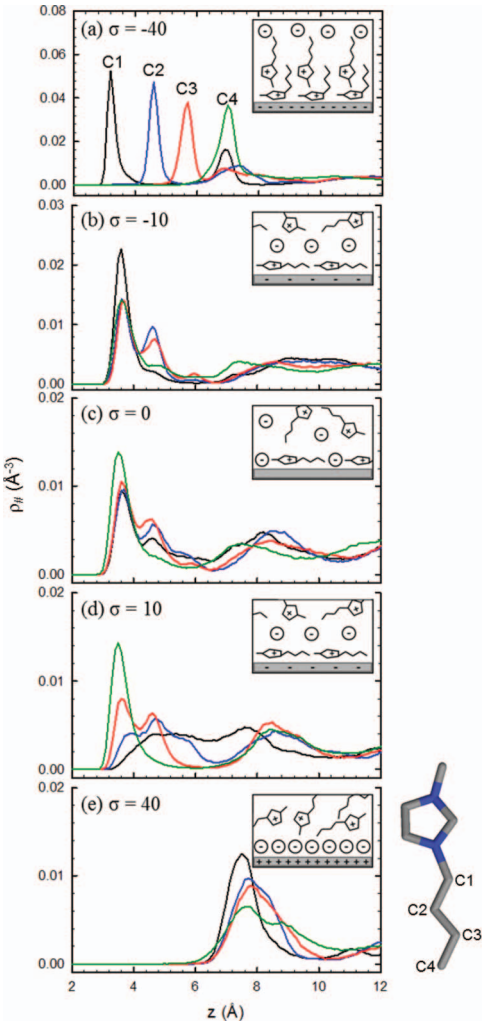

Figure 9. Number density ($\rho_{\#}$) profiles of butyl chain atoms (C1-C4) along the z-axis near graphene electrodes with different charge densities (σ) as specified (in $\mu C/cm^2$). The inset in each panel illustrates how BMIM and PF_6 ions orient near the electrode.

Figure 9 presents the number density profiles of C atoms (C1–C4) in the butyl chain, which can describe the chain orientation. The insets of Fig. 9 also illustrate how the orientations of PF_6 and BMIM change as the electrode charge varies from 0 to ± 40 $\mu C/cm^2$. When $\sigma = -10$ $\mu C/cm^2$, all four C atoms have overlapping peaks [(b)], indicating that the butyl chain is parallel to the electrode. However, when $\sigma = -40$ $\mu C/cm^2$, the chain is bent into a perpendicular orientation, as indicated by the segregated peaks in Fig. 9a. As a result, additional BMIM rings can pack in parallel into layer (a). However, rings in layer (b) cannot pack in parallel as a result of the steric interference from the butyl chain. Instead, the rings tend to pack tilted to the electrode as this is the most energetically favorable configuration. When $\sigma = 10$ $\mu C/cm^2$, the C4 peak remains close to the electrode while the other peaks shift away. As the BMIM ring is repelled from the electrode, the butyl chain rotates away from the electrode; C4, however, apparently remains anchored near the electrode due to its vdW interaction with the electrode. When $\sigma = 40$ $\mu C/cm^2$, all four peaks have shifted away, indicating that the butyl chain is no longer anchored; that space is instead occupied by PF_6.

Electric potential variations in ILs.— As demonstrated in the previous section [Fig. 5], the electrode excess surface charge (σ) creates an electric field at the surface (E_{ES}) that causes IL ions to redistribute,

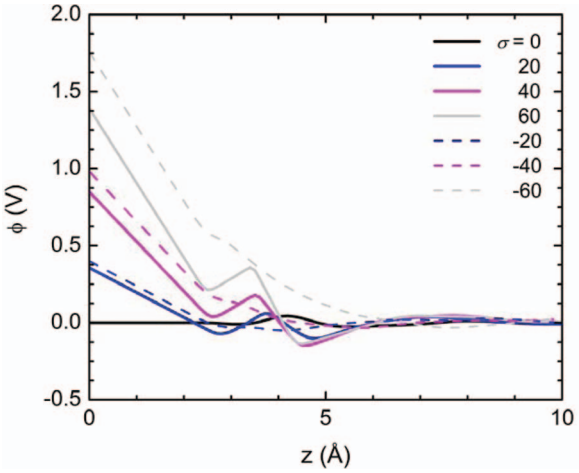

Figure 10. Potential (ϕ) profiles along the z-axis at varying excess charge densities as specified (in $\mu C/cm^2$). To facilitate comparisons, the ϕ near the negative graphene electrode is shown on a negative scale, i.e., the shown ϕ $= -\phi$. In all cases, $\phi = 0$ for the bulk electrolyte and each electrode is located at $z = 0$.

which in turn gives rise to a charge imbalance in space near the electrode. The resulting electric-potential (ϕ) profile along the surface normal direction can be obtained by solving Poisson's equation:

$$\nabla^2\phi(z) = \rho(z)/\varepsilon_0 \quad \text{with} \quad -\nabla\phi|_{ES} = E_{ES} \qquad [2]$$

where z is the distance from the electrode, ρ is the charge density averaged over a lateral z-cross section, and ε_0 is the vacuum permittivity. According to Gauss' law, $E_{ES}(\sigma)$, i.e., $E_{ES} = \sigma/\varepsilon_0$. By integrating Eq. 2, we can evaluate the potential variation in the IL electrolyte:

$$\phi(z) = -\frac{\sigma z}{\varepsilon_0} - \frac{1}{\varepsilon_0}\int_0^z (z - z')\rho(z')dz' \qquad [3]$$

Figure 10 shows calculated potential profiles near the positive [(a)] and negative [(b)] electrodes with respect to the bulk potential (which is set equal to 0 V) for various σ as specified. Here, the positive electrode position is set at $z = 0$, and a bin size of 0.1 Å was used in obtaining laterally averaged ρ(z). The results show that the potential changes mostly occur across the EDL, indicating that the accumulated counterions effectively screen E_{ES}. It is also worth noting that at a given σ, the absolute value of the potential drop ϕ_D (the electrode surface potential minus the electrolyte bulk potential) at the positive electrode side is consistently less than that of the negative electrode side. This is primarily due to the cation-anion size difference; that is, smaller PF_6 anions are packed more tightly such that E_{ES} can be screened over a smaller EDL thickness which yields a smaller $|\phi_D|$.

When $E_{ES} = 0$, the vdW interactions between the electrode and IL ions may cause a charge imbalance and consequently a potential drop in the interface region, which is the so-called potential of zero charge (PZC). For the graphene/IL system considered, the PZC turns out to be nearly 0 V, consistent with previous theoretical study;[58] recall that the number densities of BMIM and PF_6 near the electrode are very comparable. The PZC may increase as the size difference between anion and cation increases; the tighter packing of smaller ions than larger ones at the electrode-electrolyte interface can lead to differences in their number densities. Previous studies reported that the respective PZC values for [OMIM][PF_6]/graphite[58] and [BMIM][BF_4]/glassy carbon[16] could be as high as 0.15 V and 0.085 V, respectively; note that OMIM is larger in size than BMIM while BF_4 is smaller than PF_6, such that both [OMIM][PF_6] and [BMIM][BF_4] have a larger size difference than [BMIM][PF_6].

Double layer capacitance.— The capacitance of an EDL can be obtained from the relationship between σ and ϕ_D, i.e., $C = \sigma/\phi_D$ (integral) or $d\sigma/d\phi_D$ (differential). The differential capacitance is a

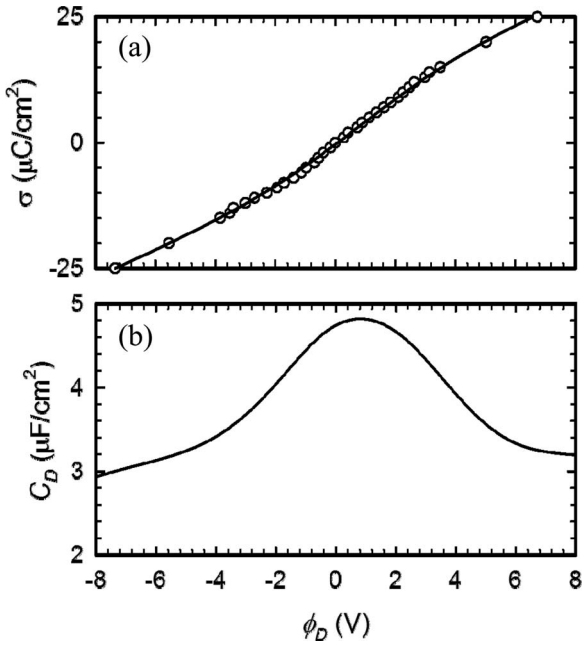

Figure 11. (a) Excess electrode charge density (σ) and (b) differential double layer capacitance (C_D) as a function of the potential drop across the EDL (ϕ_D). In (a), the circles represent data from MD simulations and the solid line is fit from smoothing the data (see Ref. 70).

measure of how the EDL microstructure responds to potential perturbations caused by a variation in σ. Hence, the differential approach is often preferred in investigating the properties of EDLs; the differential EDL capacitance (C_D) can be measured using low frequency impedance spectroscopy.[69]

Based on the σ-ϕ_D plot in Fig. 11a, we computed C_D by differentiating σ with respect to ϕ_D; the data points were smoothed using a negative exponential technique[70] for the first derivative calculation. As presented in Fig. 11b, the predicted C_D-ϕ_D curve is a convex parabola (bell shaped) with a maximum of 4.7 μF/cm^2 at $\phi_D = 0.7$ V. Here, we should point out that the value of C_D ($= d\sigma/d\phi_D$) is rather sensitive to the choice of data smoothing scheme, but the overall shape of the C_D curve tends to be more or less same. Note that the peak position appears at a positive value of ϕ_D, which is related to the difference in packing efficiency between cation and anion. That is, smaller PF_6 anions are more effectively packed than larger BMIM cations, yielding a smaller $\Delta\phi_D$ for a given $\Delta\sigma$ and consequently a larger C_D. Likewise, the C_D value monotonically decreases with increasing $|\sigma|$ (or $|\phi_D|$) due to the gradually reduced packing efficiency (as demonstrated earlier), while the PF_6 side consistently exhibits a higher C_D at a given $|\phi_D|$ than the BMIM side. It is also worth noting that the decrease of C_D becomes less steep as $|\phi_D|$ increases at both sides; this is apparently attributed to the continuing saturation of electrode surface by counterions, leading to an increase in EDL thickness as the counterions accumulate in multiple layers.

Besides such bell-shaped features,[14,71] previous experimental and theoretical studies have widely reported that the C_D curve also exhibits various camel-like shapes[15,17] in IL-electrolyte/metal-electrode systems. The shape and magnitude of C_D curve can be a complex function of multiple factors which may include polarizability of ions at the interface, size difference between cations and anions, and non-electrostatic (specific) adsorption of ions on the electrode surface. Perhaps the possible polarization of graphene and IL ions at the interface could significantly affect the electrode charge distribution, the space charge density, and thus the EDL capacitance; whereas, the effect of specific adsorption should be unimportant considering the weak adsorption of [BMIM][PF_6] ions on the pristine graphene surface.

Nonetheless, our calculations and previous other studies[14,15,17,71] unequivocally demonstrate that the C_D of EDLs decreases with increasing $|\phi_D|$ due to the reduced packing efficiency of ions; this is particularly true when $|\sigma|$ is large enough such that the electrostatic forces play a dominant role in determining the EDL structure. We should note, however, that the impact of graphene-based electrodes with structural and chemical modifications on the structure and capacitance of EDLs remains largely unknown.

Quantum capacitance.— Two-dimensional (2D) graphene-based electrodes have been found to have a quantized capacitance.[38] The quantum capacitance of graphene is defined as $C_Q = d\sigma/d\phi_G$, where $d\sigma$ and $d\phi_G$ refer to the variations of charge density and local potential in graphene, respectively. For the pristine graphene sheet, the DOS is symmetric and linear around the Fermi level (E_F). In addition, if we assume the graphene electrochemical potential μ is rigidly shifted by $e\phi_G$,[72] the excess charge density σ from the electron density (n) can be written by:

$$\sigma = e\left(n_o - n_\mu\right) = e\int_{-\infty}^{+\infty} D(E)\left[f(E) - f(E - e\phi_G)\right]dE \quad [4]$$

where $D(E)$ is the 2D DOS, $f(E)$ is the Fermi-Dirac distribution function, E is the relative energy with respect to E_F, e is the elementary charge, and the subscripts o and μ refer to the neutral and non-neutral cases, respectively. With the analytical expression of σ, the C_Q of graphene is given by:

$$C_Q = d\sigma/d\phi_G = e^2\int_{-\infty}^{+\infty} D(E)\,F_T(E-\mu)\,dE \quad [5]$$

where the thermal broadening function $[F_T(E)]$ is also expressed as $F_T(E) = -df/dE = (4kT)^{-1}\,\mathrm{sech}^2(E/2kT)$.

For the 2D graphene case, we can approximate the DOS near the Dirac point by[73]

$$D(E) \approx \frac{g_s g_v}{2\pi(\hbar v_F)^2}|E| \quad [6]$$

where g_s and g_v are the respective spin and valley degeneracies (=2), $\hbar$ is the reduced Planck's constant, and v_F is the Fermi velocity of carriers (≈10^8 cm/s).[74] Recall that $E(k)$ is approximately linear near the Dirac point.[75] The DOS of graphene can also be calculated using DFT calculations. Figure 12 presents a comparison of the DOS obtained from our DFT calculations and from Eq. 6, showing good agreement.

A few groups have recently attempted to determine the C_Q of graphene based on measurements of graphene-gated systems[36,76–78] from which the graphene C_Q is decoupled from the oxide capacitance (C_{ox}). However, the experimental C_Q values remain widely scattered and often significantly deviate from the above calculation results, especially near $\phi_G = 0$[78]. One possible source of this disagreement is

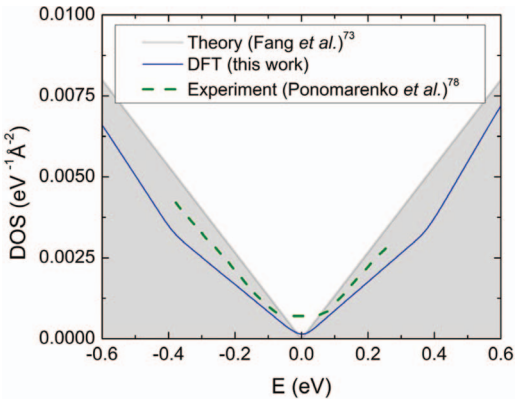

Figure 12. Comparison of pristine graphene's density of states (DOS) from theory (Ref. 73), experiment (Ref. 78), and DFT.

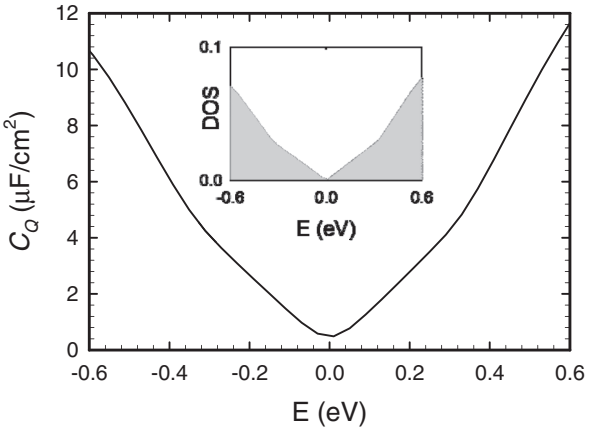

Figure 13. Calculated quantum capacitance (C_Q) of pristine graphene based on the DOS (inset). E = 0 eV indicates the position of the Fermi level.

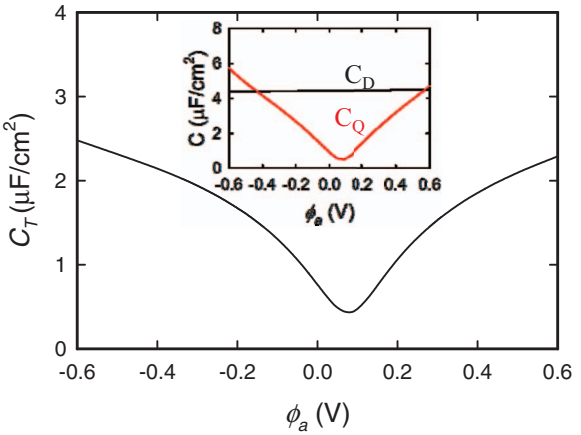

Figure 15. Total interfacial capacitance (C_T) as a function of applied potential (ϕ_a). The inset shows corresponding EDL capacitance (C_D) and quantum capacitance (C_Q).

from the estimation of C_{ox}, which is calculated either from Hall measurements or geometrically ($C_{ox} = \varepsilon_0\varepsilon_r/t_{ox}$, where t_{ox} is the oxide layer thickness). Other possible sources include defects in the graphene, the oxide surface, and/or potential fluctuations within the electrode as a result of the graphene-oxide surface interaction. As shown in Fig. 13, the calculated C_Q (300 K) for the pristine graphene based on the DOS from DFT exhibits a U-shaped curve, contrary to C_D, with a minimum around 0.58 μF/cm^2; note that $C_Q \neq 0$ when $\phi_G = 0$ due to the thermal broadening of the electron energy distribution, and as expected the C_Q curve is symmetric about $\phi_G = 0$. We should note that the possible influence of graphene-IL interactions on the DOS and C_Q have been neglected in this analysis for simplicity; however, we expect the qualitative impact of the C_Q on the total capacitance (described below) to remain the same.

Total interfacial capacitance.— The total capacitance (C_T) at the electrode/IL interface can be represented as a series of C_Q and C_D, as shown in Fig. 14, i.e., $1/C_T = 1/C_Q + 1/C_D$. With the C_Q and C_D values calculated above, we estimated C_T as a function of applied potential ϕ_a (with respect to the potential of the bulk electrolyte, i.e., $\phi_a = \phi_G + \phi_D$) as shown in Fig. 15. Here, the relationship between C_Q and C_D with ϕ_a was obtained through σ; recall that $C_Q/C_D \propto \sigma \propto \phi_G/\phi_D$. The C_T curve is U-shaped, in direct contrast to the bell-shaped C_D curve [Fig. 11b]; this is apparently attributed to the dominance of C_Q when ϕ_a is sufficiently small ($|\phi_a| < 1.0$ V). With increasing ϕ_a, the contribution of C_D becomes important. Recent experiments[16,34,35] have also broadly shown evidence for similar U-shaped C_T curves in supercapacitors based on graphite-like electrodes and IL electrolytes; some specific features such as minimum/maximum values, peak/valley positions and curvature tend to vary case by case, possibly due to the strong dependence of C_Q and C_D on the structure and purity of the carbon-based electrodes. Now it is worth pointing out that, unlike the carbon-based case, the capacitance of metal electrodes (such as platinum and gold) is much larger than C_D; hence, $C_T \approx C_D$, which could explain why the metal/IL interface mostly exhibits a bell-shaped or camel-shaped C_T curve.[14,15,17,71]

Our study clearly highlights the important role of C_Q in determining the capacitance performance of graphene-based supercapacitors. Knowing that the C_Q of graphene-like materials is directly related to the DOS, the modification of the electrode electronic structure by substitutional dopants, functional groups, and/or structural disorder/strain will significantly affect the overall capacitor performance of graphene/IL systems; however, the effect of the chemically and/or mechanically modified graphene-based electrodes still remains largely unexplored, and is, we think, an important subject for further research.

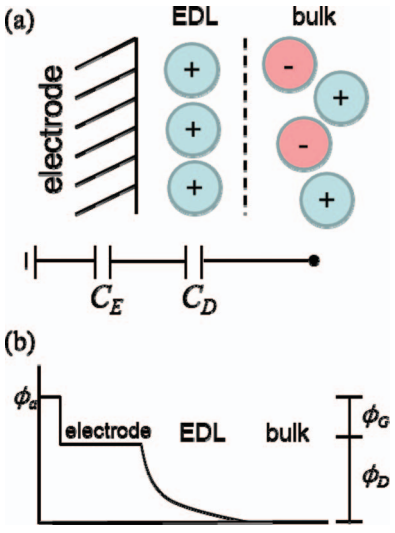

Figure 14. Schematic of the graphene/IL interface, with an illustration of the equivalent circuit with series capacitance from the electrode and double layer [(a)] and an idealized potential profile [(b)].

Summary

We evaluated the interfacial capacitance between graphene and ionic liquid (IL) [BMIM][PF_6] as a function of applied potential (ϕ_a). Here, the total capacitance (C_T) at the graphene/IL interface is given as a series of the electric double layer (EDL) capacitance (C_D) and the quantum capacitance of graphene (C_Q), i.e., $1/C_T = 1/C_D + 1/C_Q$. Using classical molecular dynamics simulations with the OPLS-AA force field, we first determined the microstructure of [BMIM][PF_6] near the graphene electrode with varying excess surface charge densities (σ = 0 to ±60 μC/cm^2), and then used the spatial ion distributions obtained to calculate the potential variations in [BMIM][PF_6] and successively EDL differential capacitances. The quantum capacitance of pristine graphene was estimated from the electronic density of states (DOS) calculated using density functional theory (DFT).

Our MD simulations clearly demonstrate the distinct alternative layering of BMIM and PF_6 in the vicinity of an electrified graphene surface, which is found to extend about 3 nm from the planar electrode while the thickness of each alternating [BMIM][PF_6] layer tends to be 7–9 Å. Analysis of the interfacial structures also shows that (i) the relatively smaller PF_6 anions are packed more densely than BMIM cations near the corresponding counter electrodes, (ii) the small and symmetric PF_6 anions pack into lattice-like structures near the counter electrode, unlike the large and complex-shaped BMIM cations,

(iii) both positive and negative electrodes tend to be overshielded by the first-layer ions unless σ is fairly large (>50 μC/cm^2), and (iv) PF_6 counterions align a plane of fluorine atoms parallel to the electrode. Similarly, BMIM counterions also tend to align parallel to the electrode; when σ > 40 μC/cm^2, the alkyl tails bend away from the electrode to allow additional packing of BMIM rings. Our results corroborate well with previous theoretical and experimental studies.

From the calculation results of potential profiles and EDL capacitances, we see that (i) the potential changes mostly occur within the first layer of counterions, providing evidence of one-ion thick compact EDL formation, (ii) the potential drop across the EDL was consistently larger at the negative electrode compared to the positive electrode, (iii) the EDL capacitance showed distinct, bell-shaped characteristics, and (iv) the capacitance of the "wings" at positive potential saturated at a higher value than at negative potential. Analysis of the EDL structure reveals that those observations are primarily attributed to differences in the size and shape of PF_6 anions and BMIM cations. While the packing efficiencies of both ions decrease with increasing |σ|, the PF_6 anion has an overall higher packing density than the BMIM cation. Note that in our calculations all atom charges were kept fixed; however, we also conceive that the shape and magnitude of the C_D curve can be a significant function of atomic polarization at the graphene/IL interface. Nonetheless, according to this work and other previous studies, it is highly plausible that the C_D of EDLs decreases with increasing |σ| due to the reduced packing efficiency of ions, resulting in bell-shaped or camel-shaped C_D curves.

The C_Q of pristine graphene calculated based on the DOS from DFT exhibits a U-shaped curve, contrary to the bell-shaped C_D, with a minimum of nearly zero. As a consequence, the C_T at the graphene/IL interface is predicted to be U-shaped (which has been also seen by previous experiments), due to the dominance of C_Q when the applied potential is sufficiently small ($|\phi_a| < 1.0$ V, while the contribution of C_D becomes important with increasing ϕ_a). Our work clearly highlights the importance of C_Q in graphene-based supercapacitors, although more sophisticated calculations might be required for improved predictions of C_D by taking into account the aforementioned atomic polarization. Note that the C_Q of graphene-based materials is directly related to the electronic structure which can be modified by substitutional dopants, functional groups, and/or structural disorder/strain. However, the impact of such chemical and/or mechanical modifications on the capacitor performance of graphene/IL systems remains largely unexplored, which warrants further investigation.

Acknowledgments

This work was supported by the R.A. Welch foundation (F-1535) and the U.S. Department of Energy, Office of Basic Energy Sciences, Division of Materials Sciences and Engineering (DE-SC001951). We thank the Texas Advanced Computing Center for use of their computing resources. Helpful discussions with Rodney S. Ruoff are also greatly acknowledged.

References

1. R. D. Rogers and K. R. Seddon, *Science*, **302**, 792 (2003).
2. W. Xu and C. A. Angell, *Science*, **302**, 422 (2003).
3. I. Krossing and J. M. Slattery, *Phys. Chem.*, **220**, 1343 (2006).
4. R. D. Rogers and G. A. Voth, *Acc. Chem. Res.*, **40**, 1077 (2007).
5. P. Simon and Y. Gogotsi, *Nat. Mater.*, **7**, 845 (2008).
6. A. Lewandowski and M. Galinski, *J. Phys. Chem. Solids*, **65**, 281 (2004).
7. S. Baldelli, *Acc. Chem. Res.*, **41**, 421 (2008).
8. M. Mezger, H. Schroder, H. Reichert, S. Schramm, J. S. Okasinski, S. Schroder, V. Honkimaki, M. Deutsch, E. M. Ocko, J. Ralston, M. Rohwerder, and M. Stratmann, *Science*, **322**, 424 (2008).
9. R. Atkin and G. G. Warr, *J. Phys. Chem. C*, **111**, 5162 (2007).
10. J. Vatamanu, O. Borodin, and G. D. Smith, *J. Phys. Chem. B*, **115**, 3073 (2011).
11. M. Bazant, B. Storey, and A. A. Kornyshev, *Phys. Rev. Lett.*, **106**, 046102 (2011).
12. R. Hayes, G. G. Warr, and R. Atkin, *Phys. Chem. Chem. Phys.*, **12**, 1709 (2010).
13. A. J. Bard and L. R. Faulkner, *Electrochemical Methods: Fundamentals and Applications*, 2nd ed., p. 551, Wiley Interscience, New York (2000).
14. Y.-Z. Su, Y.-C. Fu, J.-W. Yan, Z.-B. Chen, and B.-W. Mao, *Angew. Chem. Int. Ed.*, **48**, 5148 (2009).
15. M. T. Alam, J. Masud, M. Islam, T. Okajima, and T. Ohsaka, *J. Phys. Chem. C*, **115**, 19797 (2011).
16. M. T. Alam, M. Islam, T. Okajima, and T. Ohsaka, *J. Phys. Chem. C*, **112**, 16600 (2008).
17. V. Lockett, M. Horne, and R. Sedev, *Phys. Chem. Chem. Phys.*, **12**, 12499 (2010).
18. A. A. Kornyshev, *J. Phys. Chem. B*, **111**, 5545 (2007).
19. J. Vatamanu, O. Borodin, and G. D. Smith, *J. Am. Chem. Soc.*, **132**, 14825 (2010).
20. G. Feng, J. S. Zhang, and R. J. Qiao, *J. Phys. Chem. C*, **113**, 4549 (2009).
21. G. Feng, R. Qiao, J. Huang, S. Dai, B. G. Sumpter, and V. Meunier. *Phys. Chem. Chem. Phys.*, **13**, 1152 (2011).
22. M. V. Fedorov, N. Georgi, and A. A. Kornyshev, *Electrochem. Commun.*, **12**, 296 (2010).
23. N. Georgi, A. A. Kornyshev, and M. V. Fedorov, *J. Electroanal. Chem.*, **649**, 261 (2010).
24. Y. Lauw, M. D. Horne, T. Rodopoulos, and F. A. M. Leermakers, *Phys. Rev. Lett.*, **103**, 117801 (2009).
25. Y. Lauw, M. D. Horne, T. Rodopoulos, A. Nelson, and F. A. M. Leermakers, *J. Phys. Chem. B*, **114**, 11149 (2010).
26. Y. Shim and H. J. Kim, *ACS Nano*, **4**, 2345 (2010).
27. J. Vatamanu, L. Cao, O. Borodin, D. Bedrov, and G. D. Smith, *J. Phys. Chem. Lett.*, **2**, 2267 (2011).
28. C. Merlet, B. Rotenberg, P. A. Madden, P.-L. Taberna, P. Simon, Y. Gogotsi, and M. Salanne, *Nat. Mater.*, **11**, 1 (2012).
29. G. Feng, D. Jiang, and P. T. Cummings, *J. Chem. Theory Comput.*, **8**, 1058 (2012).
30. H. M. Jeong, J. W. Lee, W. H. Shin, Y. J. Choi, H. J. Shin, J. K. Kang, and J. W. Choi, *Nano. Lett.*, **11**, 2472 (2011).
31. D.-W. Wang, F. Li, Z.-G. Chen, G. Q. Lu, and H.-M. Cheng, *Chem. Mater.*, **20**, 7195 (2008).
32. E. Frackowiak and F. Béguin, *Carbon*, **39**, 937 (2001).
33. J.-P. Randin and E. Yeager, *J. Electrochem. Soc.*, **118**, 711 (1971).
34. J. Xia, F. Chen, J. Li, and N. Tao, *Nat. Nanotech.*, **4**, 505 (2009).
35. M. Islam, M. T. Alam, T. Okajima, and T. Ohsaka, *J. Phys. Chem. C*, **113**, 3386 (2009).
36. H. Gerischer, *J. Phys. Chem.*, **89**, 4249 (1985).
37. H. Gerischer, R. Mcintyre, D. Scherson, and W. Storck, *J. Phys. Chem.*, **91**, 1930 (1987).
38. S. Luryi, *Appl. Phys. Lett.*, **52**, 501 (1988).
39. W. L. Jorgensen, D. S. Maxwell, and J. Tirado-Rives, *J. Am. Chem. Soc.*, **118**, 11225 (1996).
40. G. Kaminski and W. L. Jorgensen, *J. Phys. Chem.*, **100**, 18010 (1996).
41. J. N. C. Lopes, J. Deschamps, and A. A. H. Pádua, *J. Phys. Chem. B*, **108**, 2038 (2004).
42. J. N. C. Lopes, J. Deschamps, and A. A. H. Pádua, *J. Phys. Chem. B*, **108**, 11250 (2004).
43. O. Borodin, G. D. Smith, and R. L. Jaffe, *J. Comput. Chem.*, **22**, 641 (2001).
44. L. Battezzati, C. Pisani, and F. Ricca, *J. Chem. Soc.*, **71**, 1629 (1975).
45. J. Kumelan, A. P.-S. Kamps, D. Tuma, and G. Maurer, *Fluid Phase Equilib.*, **228**, 207 (2005).
46. S. Maolin, Z. Fuchun, W. Guozhong, F. Haiping, W. Chunlei, C. Shimou, Z. Yi, and H. Jun, *J. Chem. Phys.*, **128**, 134504 (2008).
47. S. A. Kislenko, I. S. Samoylov, and R. H. Amirov, *Phys. Chem. Chem. Phys.*, **11**, 5584 (2009).
48. L. Verlet, *Phys. Rev.*, **159**, 98 (1967).
49. W. Hoover, *Phys. Rev. A.* **31**, 1695 (1985).
50. J. Ryckaert, G. Ciccotti, and H. J. C. Berendsen, *J. Comput. Phys.*, **23**, 327 (1977).
51. R. W. Hockney and J. W. Eastwood, *Computer Simulation Using Particles*, Adam Hilger, New York (1989).
52. I. Yeh and M. L. Berkowitz, *J. Chem. Phys.*, **111**, 3155 (1999).
53. S. J. Plimpton, *J. Comput. Phys.*, **117**, 1 (1995).
54. J. P. Perdew and Y. Wang, *Phys. Rev. B*, **45**, 13244 (1992).
55. G. Kresse and J. Furthmuller, *VASP the Guide*, Vienna University of Technology, Vienna (2001).
56. P. E. Blöchl, *Phys. Rev. B*, **50**, 17953 (1994).
57. H. J. Monkhorst and J. D. Pack, *Phys. Rev. B*, **13**, 5188 (1976).
58. S. Wang, S. Li, Z. Cao, and T. Yan, *J. Phys. Chem. C*, **114**, 990 (2010).
59. B. L. Bhargava and S. Balasubramanian, *J. Am. Chem. Soc.* **128**, 10073 (2006).
60. R. M. Lynden-Bell and M. Del Pópolo, *Phys. Chem. Chem. Phys.*, **8**, 949 (2006).
61. Y. Liu, Y. Zhang, G. Wu, and J. Hu, *J. Am. Chem. Soc.*, **128**, 7456 (2006).
62. S. Bovio, A. Podesta, C. Lenardi, and P. Milani, *J. Phys. Chem. B*, **113**, 6600 (2009).
63. The charge was calculated by numerically integrating the charge density over the length of the first layer. We defined the bounds of the layer as the two first z-positions where the total charge density = 0 coincided with the counterion number density = 0.
64. C. Pinilla, M. G. Del Pópolo, J. Kohanoff, and R. M. Lynden-Bell, *J. Phys. Chem. B*, **111**, 4877 (2007).
65. F. Tao and S. L. Bernasek, *J. Am. Chem. Soc.*, **127**, 12750 (2005).
66. The probability is equivalent to the normalized histogram of orientations. A bin size of 2° was used.
67. S. Rivera-Rubero and S. Baldelli, *J. Phys. Chem. B*, **118**, 15133 (2004).
68. C. Aliaga and S. Baldelli, *J. Phys. Chem. B*, **110**, 18481 (2006).
69. V. Lockett, R. Sedev, J. Ralston, M. Horne, and T. Rodopoulos, *J. Phys. Chem. B*, **112**, 7486 (2008).

70. The line connecting the unfilled circles was drawn by smoothing the original data points. We used a negative exponential smoothing technique embedded in SigmaPlot 12.0 to give 200 points after smoothing – the spacing between each point was 0.11 V. We then obtained the C_D at any given ϕ by numerically calculating the central difference at each point, i.e., $C_{d,i} = (\sigma_{i-2} - 8\sigma_{i-1} + 8\sigma_{i+1} - \sigma_{i+2})/12\Delta\phi$.
71. M. Islam, M. T. Alam, and T. Ohsaka, *J. Phys. Chem. C*, **112**, 16568 (2008).
72. D. L. John, L. C. Castro, and D. L. Pulfrey, *J. Appl. Phys.*, **96**, 5180 (2004).
73. T. Fang, A. Konar, H. Xing, and D. Jena, *Appl. Phys. Lett.*, **91**, 092109 (2007).
74. A. K. Geim and K. S. Novoselov, *Nature*, **6**, 183 (2007).
75. P. Wallace, *Phys. Rev.*, **329**, 622 (1947).
76. F. Giannazzo, S. Sonde, V. Raineri, and E. Rimini, *Nano Lett.*, **9**, 23 (2009).
77. S. Droscher, P. Roulleau, F. Molitor, P. Studerus, C. Stampfer, T. Ihn, and K. Ensslin, *Appl. Phys. Lett.*, **96**, 152104 (2010).
78. L. Ponomarenko, R. Yang, and R. Gorbachev, *Phys. Rev. Lett.*, **105**, 136801 (2010).